SmartScan: An intelligent scanning approach for uniform thermal distribution, reduced residual stresses and deformations in PBF additive manufacturing

Keval S. Ramani, Chuan He, Yueh-Lin Tsai, Chinedum E. Okwudire [*], Ehsan Malekipour

Department of Mechanical Engineering, University of Michigan, Ann Arbor, MI 48109, USA

ARTICLE INFO

ABSTRACT

Parts produced by laser or electron-beam powder bed fusion (PBF) additive manufacturing are prone to residual stresses, deformations, and other defects linked to non-uniform temperature distribution during the manufacturing process. Several researchers have highlighted the important role scan sequence plays in achieving uniform temperature distribution in PBF. However, scan sequence continues to be determined offline based on trial-and-error or heuristics, which are neither optimal nor generalizable. To address these weaknesses, we have articulated a vision for an intelligent scan sequence optimization approach to achieve uniform temperature distribution, hence reduced residual stresses and deformations, in PBF using physics-based and data-driven thermal models. This paper proposes SmartScan, our first attempt towards achieving our vision using a simplified physics-based thermal model. The conduction and convection dynamics of a single layer of the PBF process are modeled using the finite difference method and radial basis functions. Using the model, the next best feature (e.g., stripe or island) that minimizes a thermal uniformity metric is found using control theory. Simulations and experiments involving laser marking of a stainless steel plate are used to demonstrate the effectiveness of SmartScan in comparison to existing heuristic scan sequences for stripe and island scan patterns. In experiments, SmartScan yields up to 41% improvement in average thermal uniformity and 47% reduction in deformations (i.e., warpage) compared to existing heuristic approaches. It is also shown to be robust, and computationally efficient enough for online implementation in the future.

1. Introduction

Powder bed fusion (PBF) is an increasingly popular approach for additive manufacturing (AM) of metals (and other materials). It is used in various industries, ranging from aerospace, to automotive, to biomedical. It builds 3D parts by using a high-power source of thermal energy, typically a laser or an electron beam, to selectively fuse or melt powder layer by layer. Compared with other AM techniques for metals, PBF is popular for fabricating parts with intricate features and dense microstructure at relatively high tolerances and build rates [1,2]. However, parts produced by PBF are prone to residual stresses, deformations, and other defects linked to non-homogeneous temperature distribution during the process [1–5]. In order to mitigate these defects, post-process heat treatment is often required, which takes several hours or even days and increases the overall manufacturing costs [6]. Moreover, post-process heat treatment cannot rectify deformations or

cracking caused by residual stresses prior to being relieved. For this reason, it is preferable to avoid residual stresses and related defects as much as possible during the build process, by minimizing temperature gradients.

Several works have revealed the importance of scanning strategy in achieving uniform temperature distribution in PBF [3,4,6–9]. The term scanning strategy is often used in the literature to refer to disparate aspects of scanning in PBF. Here, we use the term in its broadest sense which includes all process parameters associated with scanning in PBF, e.g., laser or electron beam power, scan speed, hatch spacing, scan pattern and scan sequence. Scanning strategy is often selected by round-robin testing, trial and error, or heuristics [1,3]. However, given its importance in determining temperature distribution, a growing body of research is focused on controlling various elements of scanning strategy. Review articles [1,3,10] have presented comprehensive surveys on process monitoring and control in PBF. They have identified that
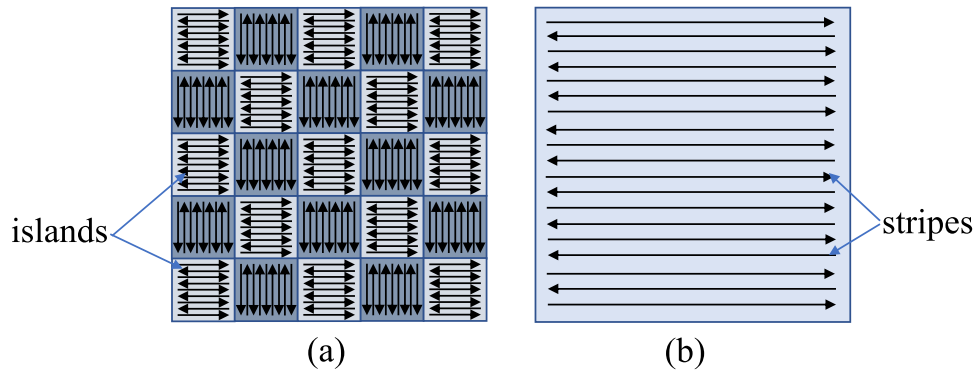

Fig. 1. Two common scan patterns for a layer in PBF: (a) island, (b) stripe. Scan sequence refers to the order in which the features (i.e., islands or stripes) of each pattern are scanned.
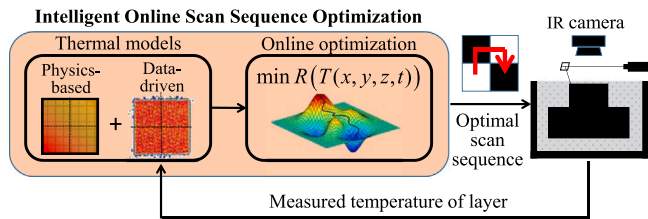

Fig. 2. Flowchart of SmartScan - an intelligent online scan sequence optimization framework [24].

beam power and scan speed are the elements of scanning strategy often controlled online or offline, e.g., [11–17]. However, Mani et al. [1] noted that there are opportunities for different control loops beyond beam power and speed.

One such opportunity that is of particular interest to the proposed work is scan sequence. Scan sequence refers to the order in which a pre-specified geometric scan pattern is traced. For example, two of the most commonly used scan patterns in practice are the stripe and island (see Fig. 1). Scan sequence in these examples could mean the order in which each line in the stripe pattern is scanned, or the order in which each island in the island pattern is scanned. Researchers have shown that scan sequence significantly affects temperature distribution, residual stresses and distortions in PBF [5,18–21].

Given the importance of scan sequence, researchers have proposed new approaches to determine scan sequence offline using heuristics. For example, in the context of the island scan pattern, Kruth et al. [21] presented the least heat influence (LHI) sequence which places the next island to be scanned as far as possible from the previously scanned islands. The LHI sequence has been shown in studies to reduce residual stresses compared to other heuristic scanning approaches, e.g., [19]. Malekipour et al. proposed a Genetic Algorithm Maximum Path (GAMP) sequence [22] which claimed to maximize the path connecting the centers of all islands using a genetic algorithm, even though no details of the algorithm were presented. Ramos et al. [20] proposed the intermittent strategy which avoids scanning adjacent islands consecutively by using a geometry-based formula having weights and radial thresholds. Using their strategy, they demonstrated significant reductions in thermally induced deformation compared to another heuristic scan sequence. However, no systematic procedure was provided for selecting the weights and thresholds in the formula, hence making it difficult to generalize. Taken together, a major weakness of existing heuristic scan sequences is that they only rely on geometric relationships that do not accurately represent the physics of temperature distribution, and they are non-generalizable. For example, it is not necessarily true that scanning islands that are furthest away from the prior scanned islands minimizes thermal gradients. It highly depends on the heat diffusion

process, which involves much more than geometry. Reiff et al. [23] presented a concept, without details, where the hotter islands from a measured or simulated temperature map of a prior layer were scanned later than the cooler islands to prevent layer-to-layer heat accumulation, which plays a major role in generating residual stresses and distortions in 3D printed parts [4]. However, this approach of selecting scan sequences is not necessarily optimal as it does not consider the transient nature of thermal distribution during scanning of the current layer.

Our research envisions an intelligent approach, dubbed SmartScan, that uses physics-based models, combined with data-driven models obtained from online thermal measurements, to efficiently determine optimal scan sequence online that minimize thermal gradients layer-by-layer [24] (see Fig. 2). Three key characteristics of SmartScan are that it is model-based, optimization-driven, and computationally efficient enough to be run online within the interlayer time of PBF processes, which is typically less than one minute. The vision of SmartScan will be achieved in phases, with increasing complexity of the models and optimization techniques adopted.

As its original contribution, this paper (and its preliminary version [25]) proposes our first attempt at achieving SmartScan using a simplified physics-based model of PBF, realized via the finite difference method (FDM) combined with radial basis functions. Using the simplified model, the next best feature (e.g., stripe or island) that minimizes a thermal uniformity metric is determined using control theory. Simulations and experiments involving laser marking of a AISI 316 L stainless steel plate are used to demonstrate the effectiveness of SmartScan in comparison to existing heuristic approaches for stripe and island scan patterns. In experiments, SmartScan yields up to 41% and 47% improvement in average thermal uniformity and deformations, respectively, compared to existing heuristic approaches. It is also shown to be robust and computationally efficient enough for future online implementation.

The rest of this paper is organized as follows: Section 2 presents the simplified thermal model used for SmartScan and the approach for determining optimal scan sequences using control theory. Section 3 presents simulation case studies, while Section 4 presents experiments performed on an open-architecture laser powder bed fusion (LPBF) machine to demonstrate the effectiveness of the proposed SmartScan approach. Section 5 concludes the paper and discusses our future work.

2. Proposed smartscan approach

This section discusses the simplified thermal modeling of the PBF process using the FDM [13], reduction of the higher-order FDM model using radial basis functions [26], and an optimization approach based on control theory to find the best scan sequence for a layer.
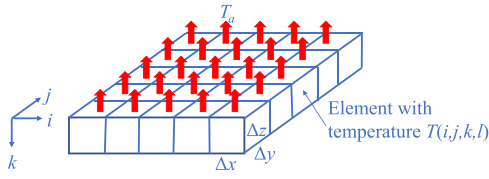
Fig. 3. Simplified finite difference model of PBF used in this paper.

2.1. Simplified Finite Difference Thermal Model and State Space Representation

In the simplified model presented in this section, a single layer of PBF is assumed. Only conductive and convective heat transfer are assumed to occur within the layer, and/or between the layer and its surroundings. Radiative heat transfer, latent heat effects, Marangoni convection, and other melt pool phenomena, are ignored. The simplified model is representative of the re-scanning process in PBF [27], or the plate marking process often used to evaluate the effects of heat accumulation and scanning strategies in PBF, e.g., [5,28]. Without loss of generality, LPBF is assumed in the rest of this paper.

Heat conduction in a medium with conductivity k_t and diffusivity α is governed by the equation

$$\frac{\partial^2 T}{\partial x^2} + \frac{\partial^2 T}{\partial y^2} + \frac{\partial^2 T}{\partial z^2} + \frac{u}{k_t} = \frac{1}{\alpha}\frac{\partial T}{\partial t} \tag{1}$$

where T is the temperature, x, y and z are the spatial coordinates, t is time and u is the power per unit volume. The FDM can be used to discretize Eq. (1) to obtain

$$\frac{T(i+1,j,k,l) + T(i-1,j,k,l) - 2T(i,j,k,l)}{\Delta x^2}$$
$$+ \frac{T(i,j+1,k,l) + T(i,j-1,k,l) - 2T(i,j,k,l)}{\Delta y^2}$$
$$+ \frac{T(i,j,k+1,l) + T(i,j,k-1,l) - 2T(i,j,k,l)}{\Delta z^2}$$
$$+ \frac{u(i,j,k,l)}{k_t} = \frac{1}{\alpha}\frac{T(i,j,k,l+1) - T(i,j,k,l)}{\Delta t} \tag{2}$$

where Δx, Δy and Δz are the dimensions of each element (see Fig. 3), i, j and k are the spatial indices of the elements, l is the temporal index (i.e., $t = l\Delta t$), Δt is the time step and $T(i,j,k,l)$ is the temperature of the element located at (i,j,k) at time l. Rearranging Eq. (2) gives the state equation

$$\mathbf{T}(l+1) = \mathbf{A}\mathbf{T}(l) + \mathbf{B}\mathbf{u}(l) \tag{3}$$

where $\mathbf{T}(l)$ is the state vector comprising the temperatures of all n_e elements of the model at time l, $\mathbf{A}$ is the state matrix, $\mathbf{B}$ is the input matrix and $\mathbf{u}(l)$ denotes the power input to the elements at time l. The vector $\mathbf{u}(l)$ is sparse. Only elements experiencing the effect of the laser heat at any given time l have non-zero values of $\mathbf{u}(l)$. In this paper, we assume that the laser heats one element at a time. Hence only one member of the vector $\mathbf{u}(l)$ has a non-zero value at any given time. The heat flux of the laser beam is described by a Gaussian profile [20] given by

$$Q(r_b, \theta) = \frac{2\lambda P}{\pi R_b^2} e^{-\frac{2r_b^2}{R_b^2}} \tag{4}$$

where Q, λ, P, R_b and r_b are the heat flux, absorptance, laser power, laser beam spot radius and distance to the beam center, respectively. Eq. (4) is integrated over the beam area and the equivalent heat is applied uniformly over the area of the heated element.

The FDM is an excellent method for developing our simplified model for SmartScan because it is versatile. It can accommodate arbitrary layer geometries and allow for a variety of boundary conditions, e.g., con-
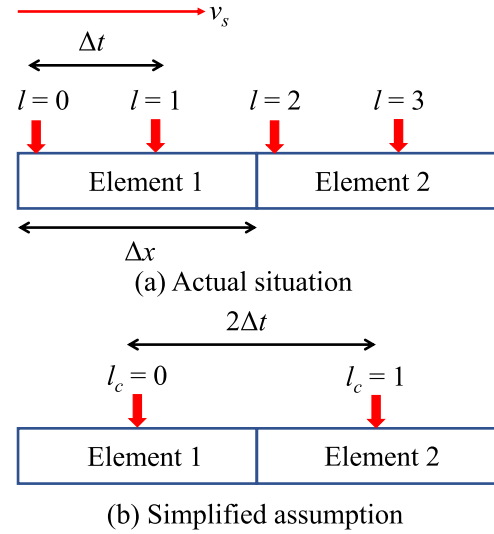

Fig. 4. Diagram depicting the assumption that the laser heat acts at the center of each element (for a sample case where $n_c = 2$): (a) actual situation, (b) simplified assumption.

vection, isothermal or adiabatic. For example, convection at the top surface can be incorporated into the model using the heat sink solution [29] as shown in Fig. 3. The power per unit volume term in Eq. (2) for the top-surface elements can be expressed as

$$u(i,j,1,l) = u_s(i,j,1,l) - u_{conv}(i,j,1,l) \tag{5}$$

where u_s and u_{conv} respectively denote the contributions of the laser source and convection to the total power for the element. The convection term can be expressed as

$$u_{conv}(i,j,1,l) = \frac{h}{\Delta z}(T(i,j,1,l) - T_a) \tag{6}$$

where h and T_a denote the convection coefficient and ambient temperature, respectively. The power due to convection can be easily embedded into the $\mathbf{A}\mathbf{T}(l)$ term of the state equation (Eq. (3)) by incorporating an additional state T_a that does not vary with time. A similar process can be applied to any surface of the model.

Typical scan patterns, such as stripe or island, consist of simple constant velocity (v_s) and constant power (P) lines, and each line can be visualized as heating of a one-dimensional array of FDM elements. Our simplified FDM model assumes that the laser heat on an element acts at the center of the element (as shown in Fig. 4). The number of time steps spent on an element can be approximated as

$$n_c \approx \frac{\Delta x}{v_s \Delta t} \tag{7}$$

The corresponding state equation for heating of an element can then be written as

$$\mathbf{T}(l_c + 1) = \mathbf{A}_c \mathbf{T}(l_c) + \mathbf{b}_c;$$
$$\mathbf{A}_c \triangleq \mathbf{A}^{n_c}; \; \mathbf{b}_c \triangleq \sum_{m=0}^{n_c-1} \mathbf{A}^m \mathbf{B}\mathbf{u}(m); l_c = n_c l \tag{8}$$

Note that, different from Eq. (3), the state-space model of Eq. (8) has a sampling interval of $n_c \Delta t$ (see Fig. 4). Similarly, this idea can be extended to any feature (e.g., stripe or island) of a scan pattern to obtain a feature-level state-space representation given by

$$\mathbf{T}(l_p + 1) = \mathbf{A}_p \mathbf{T}(l_p) + \mathbf{b}_p;$$
$$\mathbf{A}_p \triangleq \mathbf{A}^{n_p}; \; \mathbf{b}_p \triangleq \sum_{m=0}^{n_p-1} \mathbf{A}^m \mathbf{B}\mathbf{u}(m); \; l_p = n_p l \tag{9}$$

where n_p is the number of time steps required to trace a feature (e.g., stripe or island) of the pattern. Note that the state equation given by Eq. (9) has a sampling time $n_p\Delta t$.

Remark 1: Notice that the point-to-point positioning time of the laser is not included in the formulation above because it is negligible compared to the time spent scanning, as observed by Mugwagwa et al. [5]. This is because the point-to-point positioning speed (also known as jump speed) is typically 5–10 times higher than the scanning speed. Also, it is assumed in Eq. (9) that the number of time steps needed to scan each feature is constant. This is often the case with stripe and island patterns of fixed dimension.

2.2. Model Reduction using Radial Basis Functions

Computation and optimization using the FDM model can become cumbersome as the number of elements/states grow (for example, due to an increase in the size of the layer or the addition of a substrate to the model). This section describes the use of radial basis functions to reduce the higher-order FDM model. Radial basis functions have been used for thermal modeling of PBF in the literature, e.g., [30].

For any given time step, l, the temperature T at location (i,j,k) can be expressed using radial basis functions [26] as follows

$$T(i,j,k) = \sum_{p=1}^{s} w_p \varphi(r_p); \varphi(r_p) = e^{-(\varepsilon r_p)^2}; r_p \triangleq \left\| \begin{bmatrix} i \\ j \\ k \end{bmatrix} - \begin{bmatrix} i_p \\ j_p \\ k_p \end{bmatrix} \right\|_2 \quad (10)$$

where ε is the shape parameter; φ is the radial basis function, $[i_p \, j_p \, k_p]^T$ is the location of the representation elements; s is the number of representation elements; and r_p ($p = 1, 2, …, s$) is the Euclidean distance between the element at (i, j, k) and the representation element (i_p, j_p, k_p). In the matrix form, Eq. (10) can be expressed as

$$T(i,j,k) = \underbrace{\begin{bmatrix} \varphi(r_1) & \varphi(r_2) & … & \varphi(r_s) \end{bmatrix}}_{\mathbf{m}} \begin{bmatrix} w_1 \\ w_2 \\ \vdots \\ w_s \end{bmatrix} \quad (11)$$

If we consider the temperature of all elements in a layer, the state vector $\mathbf{T}$ (from Eq. (9)) can be expressed as

$$\mathbf{T}(l_p + 1) = \mathbf{M}_t \mathbf{W} \quad (12)$$

where $\mathbf{W} = [w_1 \, w_2 \, … \, w_s]^T$ and $\mathbf{M}_t$ is obtained by aggregating $\mathbf{m}$ for all elements in the model. The coefficients w_p are obtained by enforcing the interpolation conditions at the representation elements and solving the system of linear equations

$$\underbrace{\begin{bmatrix} \varphi(r_{11}) & \varphi(r_{12}) & … & \varphi(r_{1s}) \\ \varphi(r_{21}) & \varphi(r_{22}) & … & \varphi(r_{2s}) \\ \vdots & \vdots & \ddots & \vdots \\ \varphi(r_{s1}) & \varphi(r_{s2}) & … & \varphi(r_{ss}) \end{bmatrix}}_{\mathbf{M}_r} \underbrace{\begin{bmatrix} w_1 \\ w_2 \\ \vdots \\ w_s \end{bmatrix}}_{\mathbf{W}} = \underbrace{\begin{bmatrix} T(i_1, j_1, k_1) \\ T(i_2, j_2, k_2) \\ \vdots \\ T(i_s, j_s, k_s) \end{bmatrix}}_{\mathbf{T}_r} \quad (13)$$

where r_{pq} is the Euclidean distance between elements (i_p, j_p, k_p) and (i_q, j_q, k_q). The solution to the linear equation is given by

$$\mathbf{W} = \mathbf{M}_r^{-1} \mathbf{T}_r \quad (14)$$

Substituting Eq. (14) into Eq. (12) gives

$$\mathbf{T}(l_p + 1) = \underbrace{\mathbf{M}_t \mathbf{M}_r^{-1}}_{\Sigma} \mathbf{T}_r(l_p + 1) = \Sigma \mathbf{T}_r(l_p + 1) \quad (15)$$

Substituting Eq. (15) into Eq. (9) gives

$$\Sigma \mathbf{T}_r(l_p + 1) = \mathbf{A}_p \Sigma \mathbf{T}_r(l_p) + \mathbf{b}_p \quad (16)$$

Pre-multiplying Eq. (16) by Ω (where Ω is the pseudoinverse of Σ)

gives

$$\underbrace{\Omega\Sigma}_{=\mathbf{I}} \mathbf{T}_r(l_p + 1) = \underbrace{\Omega\mathbf{A}_p\Sigma}_{\widetilde{\mathbf{A}}_p} \mathbf{T}_r(l_p) + \underbrace{\Omega\mathbf{b}_p}_{\widetilde{\mathbf{b}}_p} \quad (17)$$

where $\mathbf{I}$ is the identity matrix. Hence, the transformed (reduced) state-space equation using radial basis functions is given by

$$\mathbf{T}_r(l_p + 1) = \widetilde{\mathbf{A}}_p \mathbf{T}_r(l_p) + \widetilde{\mathbf{b}}_p \quad (18)$$

Remark 2: Eq. (18) has reduced the FDM model from the total number of n_e elements in the original formulation in Eq. (9) to the s number of representation elements, where $s << n_e$. This will enable more efficient computation and optimization for larger models.

2.3. Scan Sequence Optimization using Control Theory

Based on the assumption that each layer in LPBF can be divided into similar features, such as stripes or islands, for the purpose of scanning (see Fig. 1), the objective is to find an optimal scan sequence such that at the end of scanning each feature the following temperature uniformity metric $R(l_p)$ is minimized

$$R(l_p) = \sqrt{\frac{\sum_{i,j,k}\left(T_r(i,j,k,l_p) - T_{r,avg}(l_p)\right)^2}{sT_m^2}} \quad (19)$$

where $T_{r,avg}(l_p)$ is the average temperature of representation elements $T_r(i,j,k,l_p)$ at time l_p and T_m is the melting temperature of the material. Note that the definition of $R(l_p)$ is altered slightly from that used in [19] by adopting the melting temperature of the material in the denominator, rather than the average temperature. A smaller value of $R(l_p)$ implies a more uniform temperature distribution. Notice that $R(l_p)$ is a function of the state vector $\mathbf{T}_r(l_p)$ and can be expressed as

$$R(l_p) = \|\mathbf{C}_{eq}\mathbf{T}_r(l_p)\|_2;$$
$$\mathbf{C}_{eq} = \frac{1}{\sqrt{s}T_m}\left[\mathbf{I} - \frac{\mathbf{1}\mathbf{1}^T}{s} \quad \mathbf{0}\right] \quad (20)$$

where $\mathbf{I}$ is the identity matrix, $\mathbf{1}$ is a row vector whose elements are all equal to 1, and $\mathbf{0}$ is a null matrix used to account for any elements of $T_r(l_p)$ that are not needed to calculate $R(l_p)$ – e.g., T_a. The optimization problem can be formulated as

$$\min_{\mathbf{u}_{eq}(l_p)} \left(R(l_p + 1) = \|\mathbf{C}_{eq}\mathbf{T}_r(l_p + 1)\|_2\right)$$
$$\text{s.t.} \, \mathbf{T}_r(l_p + 1) = \mathbf{A}_{eq}\mathbf{T}_r(l_p) + \mathbf{B}_{eq}\mathbf{u}_{eq}(l_p) \quad (21)$$

where $\mathbf{A}_{eq} = \widetilde{\mathbf{A}}_p$, the columns of $\mathbf{B}_{eq}$ represent corresponding vectors $\widetilde{\mathbf{b}}_p$ (see Eq. (18)) for each feature and $\mathbf{u}_{eq}(l_p)$ is a vector consisting of only one element equal to 1 and all other elements equal to 0. The location of 1 in $\mathbf{u}_{eq}(l_p)$ represents the column of $\mathbf{B}_{eq}$ and, hence, the feature to be scanned. The objective of the optimization problem can be written as

$$\|\mathbf{C}_{eq}\mathbf{T}_r(l_p + 1)\|_2^2$$
$$= \|\mathbf{C}_{eq}\mathbf{A}_{eq}\mathbf{T}_r(l_p) + \mathbf{C}_{eq}\mathbf{B}_{eq}\mathbf{u}_{eq}(l_p)\|_2^2$$
$$= \mathbf{u}_{eq}^T(l_p)\mathbf{B}_{eq}^T\mathbf{C}_{eq}^T\mathbf{C}_{eq}\mathbf{B}_{eq}\mathbf{u}_{eq}(l_p)$$
$$+ 2\mathbf{T}_r^T(l_p)\mathbf{A}_{eq}^T\mathbf{C}_{eq}^T\mathbf{C}_{eq}\mathbf{B}_{eq}\mathbf{u}_{eq}(l_p)$$
$$+ \mathbf{T}_r^T(l_p)\mathbf{A}_{eq}^T\mathbf{C}_{eq}^T\mathbf{C}_{eq}\mathbf{A}_{eq}\mathbf{T}_r(l_p) \quad (22)$$

The last term of the summation in Eq. (22) is independent of $\mathbf{u}_{eq}(l_p)$, thus it does not affect the optimization. The vector $\mathbf{u}_{eq}(l_p)$ has one element equal to 1 and all others equal to 0 which results in only the diagonal terms of $\mathbf{B}_{eq}^T\mathbf{C}_{eq}^T\mathbf{C}_{eq}\mathbf{B}_{eq}$ affecting the summation. Hence, the optimization problem can be reformulated as
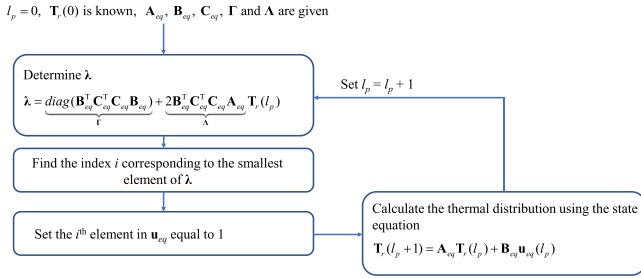
$l_p = 0$, $\mathbf{T}_r(0)$ is known, $\mathbf{A}_{eq}$, $\mathbf{B}_{eq}$, $\mathbf{C}_{eq}$, $\boldsymbol{\Gamma}$ and $\boldsymbol{\Lambda}$ are given

Determine $\boldsymbol{\lambda}$

$$\boldsymbol{\lambda} = \underbrace{diag(\mathbf{B}_{eq}^{\mathrm{T}}\mathbf{C}_{eq}^{\mathrm{T}}\mathbf{C}_{eq}\mathbf{B}_{eq})}_{\boldsymbol{\Gamma}} + \underbrace{2\mathbf{B}_{eq}^{\mathrm{T}}\mathbf{C}_{eq}^{\mathrm{T}}\mathbf{C}_{eq}\mathbf{A}_{eq}\mathbf{T}_r(l_p)}_{\boldsymbol{\Lambda}}$$

Set $l_p = l_p + 1$

Find the index i corresponding to the smallest element of $\boldsymbol{\lambda}$

Set the ith element in $\mathbf{u}_{eq}$ equal to 1

Calculate the thermal distribution using the state equation

$$\mathbf{T}_r(l_p + 1) = \mathbf{A}_{eq}\mathbf{T}_r(l_p) + \mathbf{B}_{eq}\mathbf{u}_{eq}(l_p)$$

Fig. 5. Flowchart of the proposed SmartScan.

Table 1
Parameters used in simulations (and experiments).

Parameter, symbol (Units)	Value
Laser power, P (W)	200
Laser spot diameter, $2R_b$ (μm)	77
Absorptance, λ[32]	0.37
Mark/scan speed, v_s (mm/s)	600
Hatch spacing (μm)	200
Conductivity, k_t (W/(mK))[33]	22.5
Diffusivity, α (m^2/s)[33]	5.632×10^{-6}
Melting temperature, T_m (K)[33]	1658
Convection coefficient, h (W/(m^{2}K))[31]	25
Initial temperature, $T(x,y,z,0)$ (K)	293
Ambient temperature, T_a (K)	293

$$\min_i \lambda_i$$

$$\text{s.t.}\, \boldsymbol{\lambda} = \underbrace{diag\left(\mathbf{B}_{eq}^{\mathrm{T}}\mathbf{C}_{eq}^{\mathrm{T}}\mathbf{C}_{eq}\mathbf{B}_{eq}\right)}_{\boldsymbol{\Gamma}} + \underbrace{2\mathbf{B}_{eq}^{\mathrm{T}}\mathbf{C}_{eq}^{\mathrm{T}}\mathbf{C}_{eq}\mathbf{A}_{eq}}_{\boldsymbol{\Lambda}}\mathbf{T}_r\left(l_p\right) \qquad (23)$$

where λ_i are the elements of $\boldsymbol{\lambda}$. Since $\boldsymbol{\Gamma}$ and $\boldsymbol{\Lambda}$ are known a priori, they can be pre-computed offline. Accordingly, the process for determining optimal scan sequence using the proposed SmartScan is summarized in Fig. 5.

Remark 3: The total computation time for SmartScan can be divided into online (comprising of computations that need to be performed online during the interlayer time as seen in Fig. 5) and offline computations of the constant matrices in Fig. 5. As demonstrated in Sections 3 and 4, currently the SmartScan approach considers only one layer and is implemented offline. However, in the future multiple layers will be considered and SmartScan will be implemented online.

3. Numerical evaluation of smartscan

3.1. Comparative Evaluation of Thermal Uniformity

Here, we demonstrate the effectiveness of the proposed SmartScan approach in terms of optimizing thermal distribution using two case studies: (1) an island scan pattern (see Fig. 1(a)); and (2) a stripe scan pattern (see Fig. 1(b)). In both cases, we assume that an area of 5 cm × 5 cm is scanned in the middle of a solid AISI 316 L stainless steel plate with a length of 6 cm, a width of 6 cm and a thickness of 1 mm (a similar set up is used for experiments in Section 4). The FDM model has two layers. The first layer has a thickness of $\Delta z = 200$ μm (representing the scanned layer) and a second layer of thickness 800 μm, representing the rest of the plate's thickness. For both layers, $\Delta x = \Delta y = 200$ μm (resulting in 300 × 300 elements per layer; hence the total number of elements in the model, $n_e = 180,000$). The time step Δt is selected as 0.333 ms. The top and bottom surfaces of the plate experience convection whereas the peripheral surfaces are assumed to have adiabatic boundary conditions, due to their negligible surface areas. The RBF representation elements are evenly distributed (60 × 60) across the top layer, with a shape parameter of $\varepsilon = 0.8$; hence $s = 3600$. The parameters for the thermal model are summarized in Table 1. Note that the absorptance, conductivity, diffusivity and melting temperature are obtained from the references cited in the table for AISI 316 L stainless steel (under solidus conditions, where relevant). Some of the material properties mentioned in Table 1 vary with temperature and other factors. Our simulations assume constant values for these properties, as tabulated in Table 1, and Section 3.2 explores the robustness of the SmartScan approach with regards to variations in key material properties. The convection coefficient for a surface under still air is obtained from Ref. [31]. The other parameters in the table correspond to those used in experiments in Section 4.

3.1.1. Case 1: Island Scan Pattern

For this case study, the 5 cm × 5 cm area to be scanned is divided into 100 (0.5 cm × 0.5 cm) islands numbered from 1 to 100 as shown in Fig. 6(a). As is typical [5,21], the direction of the scan vectors within each island is rotated by 90° for the even numbered islands relative to the odd numbered islands (see Fig. 1(a)). Three common heuristic
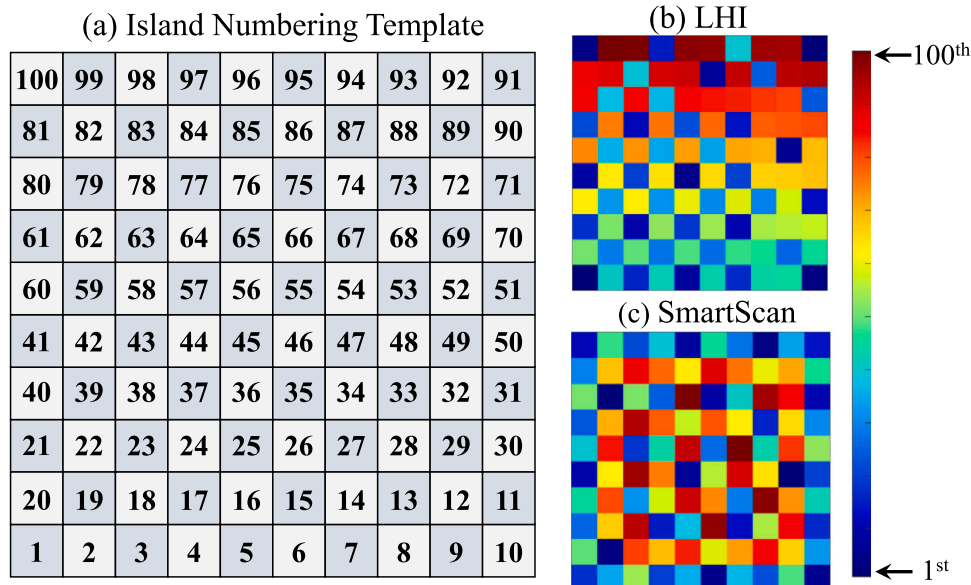
(a) Island Numbering Template

100	99	98	97	96	95	94	93	92	91
81	82	83	84	85	86	87	88	89	90
80	79	78	77	76	75	74	73	72	71
61	62	63	64	65	66	67	68	69	70
60	59	58	57	56	55	54	53	52	51
41	42	43	44	45	46	47	48	49	50
40	39	38	37	36	35	34	33	32	31
21	22	23	24	25	26	27	28	29	30
20	19	18	17	16	15	14	13	12	11
1	2	3	4	5	6	7	8	9	10

(b) LHI

(c) SmartScan

← 100th

← 1st

Fig. 6. (a) Island numbering template; and color maps of island scan sequences for (b) LHI and (c) Proposed SmartScan approaches.
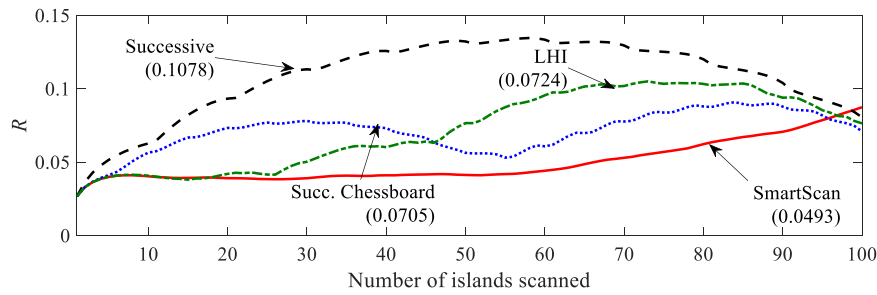
Fig. 7. Simulated thermal uniformity metric (*R*) for different scan sequences as a function of the number of islands scanned. The numbers in parenthesis show the mean value of *R* for each scan sequence.
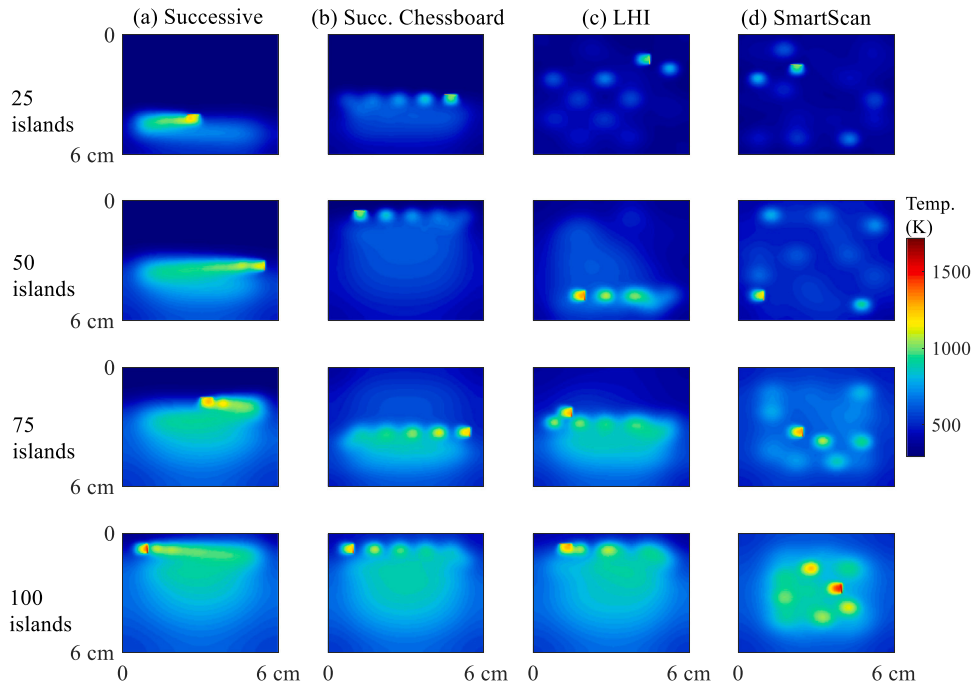

Fig. 8. Simulated temperature distribution of 6 cm × 6 cm AISI 316 L stainless steel plate for island scan pattern at four instances during the scanning process. The proposed SmartScan shows more uniform temperature distribution than the competing heuristic approaches.

sequences, namely: Successive (i.e., 1, 2, 3, ..., 100), Successive Chessboard (i.e., 1, 3, 5, ..., 99, 2, 4, 6, ..., 100), and LHI, are used as benchmarks to evaluate the proposed SmartScan approach. The LHI approach used in our numerical study is based on the tessellation algorithm proposed by Malekipour [19] because it provided an unambiguous description of its working principle and input variables, thus making it straightforward to be reproduced. The tessellation algorithm

Fig. 9. Color map of SmartScan sequence for the stripe pattern.

maximizes the pairwise Euclidean distance between the next island to be scanned and each of the already scanned islands (as shown in the color map of Fig. 6(b)). The first ten entries of the LHI sequence are: 1, 91, 10, 100, 45, 52, 86, 5, 41 and 23; the full LHI sequence is provided in the Appendix. Note that there is a large set of solutions that meet the condition of the tessellation algorithm, but it has no mechanism to select the optimal solution from the set of possible solutions. As a result, several islands were scanned in close proximity to one another towards the end of the scanning process (see Fig. 6(b)). Fig. 6(c) shows a color map of the optimal sequence determined by the proposed SmartScan approach. Its first ten entries are: 49, 79, 19, 93, 6, 10, 45, 96, 75, and 41; the full SmartScan sequence is provided in the Appendix. Notice that it is difficult – if not impossible – to decipher the SmartScan sequence via intuition or heuristics because it is model-based and optimization-driven.
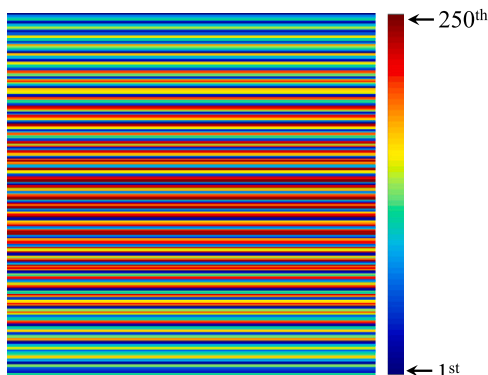
Fig. 7 shows the temperature uniformity metric, *R*, defined in Eq. (19) as a function of the number of islands scanned. Observe that SmartScan performs much better than the Successive, Successive Chessboard and LHI scan sequences. The value of *R* is calculated based on the 6 cm × 6 cm scanned area, i.e., the entire plate. The mean value of *R* is reported in Fig. 7. SmartScan yields 2.19, 1.43 and 1.47 times (or 54.2%, 30.1% and 31.9%) lower mean *R* than the Successive, Successive Chessboard and LHI approaches, respectively. This indicates that the
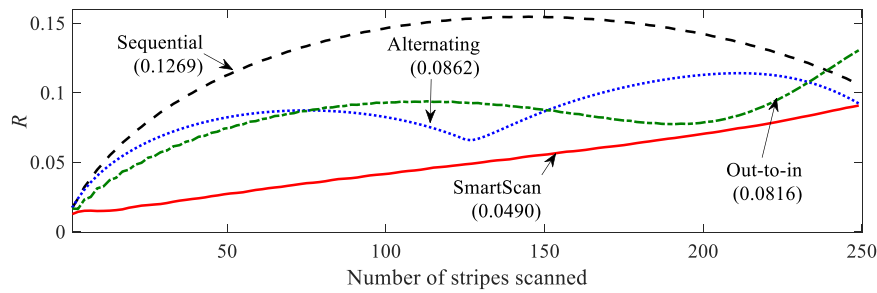
Fig. 10. Simulated thermal uniformity metric (R) for different scan sequences as a function of number of stripes scanned. The numbers in parentheses show the mean value of R for each scan sequence. The proposed SmartScan shows more uniform temperature distribution than the competing heuristic approaches.
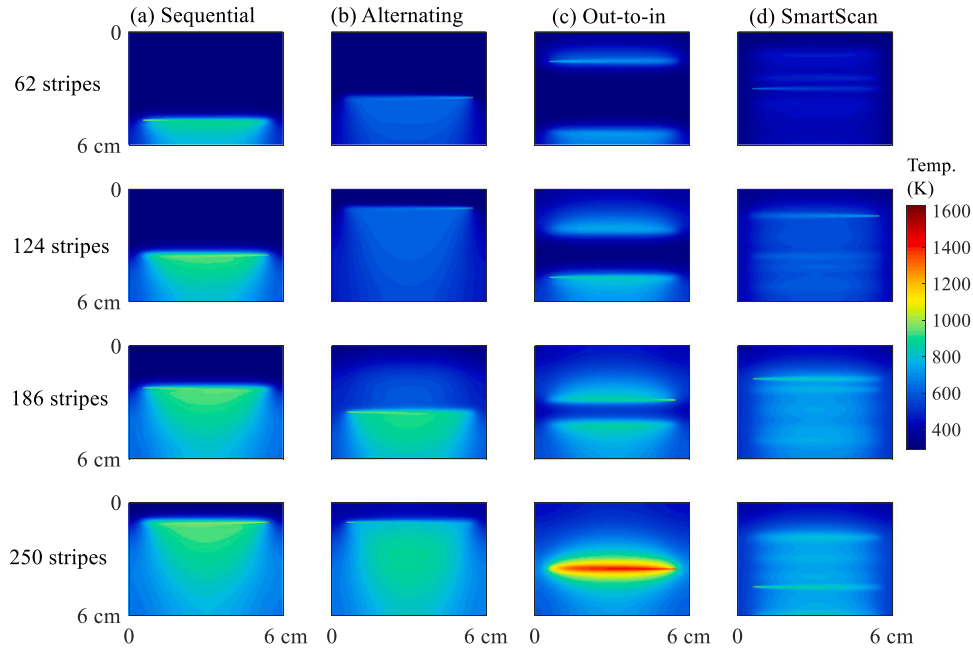

Fig. 11. Simulated temperature distribution of 6 cm × 6 cm AISI 316 L stainless steel plate for stripe scan pattern at four instances during the scanning process. The proposed SmartScan shows more uniform temperature distribution than the competing heuristic approaches.

proposed SmartScan sequence yields better thermal uniformity compared to the competing approaches. This fact is confirmed by Fig. 8 which shows the thermal distribution of the four approaches at four instances – after 25, 50, 75 and 100 islands are scanned (see the supplemental information for.gif animations of the temperature distribution of each sequence as a function of time). SmartScan generally shows better temperature distribution than the heuristic approaches at all instances except at the beginning and at the end of the scanning process where all methods show very similar uniformity.

3.1.2. Case 2: Stripe Scan Pattern

For this case study, the 5 cm × 5 cm area to be scanned is divided into 250 stripes numbered sequentially from 1 at the bottom edge to 250 at the top edge of the scanned area. The first ten sequences of SmartScan are: 250, 1, 27, 51, 75, 224, 200, 176, 152 and 12; the full SmartScan sequence is depicted using a color map in Fig. 9 and is listed in the Appendix. Notice that, as with the island case, the stripe SmartScan sequence is difficult – if not impossible – to decipher via intuition or heuristics because it is model-based and optimization-driven. It is compared with common heuristic stripe sequences, namely, the Sequential (1, 2, 3, …, 250), Alternating (1, 3, …, 249, 2, 4, …, 250) and Out-to-in (1, 250, 2, 249, …125,126) approaches. Fig. 10 shows the temperature uniformity metric as a function of number of stripes scanned. The mean value of R is reported in Fig. 10. The proposed optimal

Table 2
Online computation time and mean R values as the number of representation elements are varied for island and stripe cases.

Number of representation elements	Island		Stripe	
	Online computation time [s]	Mean R value	Online computation time [s]	Mean R value
40 × 40	2	0.0692	3	0.0721
60 × 60	6	0.0493	8	0.0490
80 × 80	13	0.0485	15	0.0452

approach yields 2.59, 1.76 and 1.67 times (or 61.4%, 43.2% and 40.0%) lower mean R value than the Sequential, Alternating and Out-to-in approaches, respectively. This fact is confirmed by Fig. 11 which shows the thermal distribution of the four approaches at four instances – after 62, 124, 186 and 250 stripes are scanned (see the supplemental information for.gif animations of the temperature distribution of each sequence as a function of time). SmartScan generally shows better temperature distribution than the heuristic approaches at all instances.

Table 3

Mean R values as functions of errors in conductivity, convection coefficient and absorptivity for island and stripe cases.

% Error	Mean R value					
	Conductivity		Convection Coefficient		Absorptivity	
	Island	Stripe	Island	Stripe	Island	Stripe
-10%	0.0511	0.0503	0.0492	0.0491	0.0493	0.0488
-5%	0.0503	0.0495	0.0492	0.0490	0.0489	0.0497
0%	0.0493	0.0490	0.0493	0.0490	0.0493	0.0490
5%	0.0488	0.0478	0.0493	0.0490	0.0490	0.0492
10%	0.0487	0.0476	0.0499	0.0492	0.0490	0.0486

3.2. Evaluation of Computational Efficiency and Robustness of SmartScan

Firstly, in this section we seek to elucidate the tradeoff between temperature uniformity and computational efficiency as the number of radial basis functions used in the proposed SmartScan approach are varied. Table 2 shows the online computation time (see Remark 3) and mean R values as the number of representation elements are varied for both the island and stripe cases. The computations are performed on a computer with a Xeon E-2136 6 C 3.30 GHz processor, Z Turbo Drive 512 GB SSD drive and 32 GB RAM. It is observed that increasing the number of representation elements from 40×40 to 60×60 improves the temperature uniformity by more than 30% at the expense of about 3 times increase in the online computation time. Increasing the representation elements to 80×80 from 60×60 results over 2 times increase in the computational time but the resultant improvement in temperature uniformity is less than 8%. This fact demonstrates that 60×60 representation elements achieve a good tradeoff between accuracy and computation time. Therefore, 60×60 representation elements were used for the simulations in Section 3.1 and the experiments in Section 4.2.

Remark 4: For Cases 1 and 2, described in Section 3.1, it takes only 6 and 8 s, respectively, for the online computation of the optimal scan sequences following the process outlined in Fig. 5, after the constant matrices (e.g., $\mathbf{\Gamma}$ and $\mathbf{\Lambda}$) have been pre-computed offline. This implies that the proposed SmartScan approach is computationally efficient enough to be computed within the interlayer time of PBF and can be implemented online in future (see Remark 3).

Secondly, in this section, we seek to explore the robustness of SmartScan with respect to simulation parameters like conductivity, convection coefficient and absorptivity, which were obtained from generic references, hence are subject to uncertainty. Also, some of these properties are temperature dependent and might change during the scanning process. Note that since diffusivity is proportional to conductivity, its uncertainty is considered along with that of conductivity. Table 3 shows the mean R values for different percentage errors in conductivity, convection coefficient and absorptivity for both the island and stripe cases. The maximum variations in thermal uniformity with respect to a maximum of $\pm 10\%$ error in conductivity, convection coefficient and absorptivity are 3.7%, 1.2% and 1.4%, respectively. This example shows that SmartScan is reasonably robust with respect to parametric errors. The implication is that very precise calibration of model parameters may not be needed for the proposed SmartScan.

4. Experimental evaluation of SmartScan

4.1. Experimental Setup and Procedure

To evaluate the effectiveness of SmartScan in experiments, a similar setup and case studies as used in the simulations reported in Section 3 were adopted. The experiments were conducted using the open-architecture PANDA 11 LPBF machine (from OpenAdditive, LLC, Beavercreek, OH) shown in Fig. 12 (a). The machine is equipped with a 500 W IPG Photonics 1070 nm fiber laser combined with a SCANLAB hurrySCAN galvo scanner with an F-theta lens on its z-stage. It is controlled using the Open Machine Control software that allows custom scan patterns and scan sequences to be programmed by a user using macros. The PANDA 11 was retrofitted with an Optris PI 640 G7 IR camera with 33° x 25° lens/ $f = 18.7$ mm, capable of capturing thermal images over temperature ranges from $-20\,°C$ to $1500\,°C$ at frame rates of up to 125 Hz.

The experiments involved marking a 5 cm $\times$ 5 cm area on AISI 316 L stainless steel (SS) plates of dimensions L $\times$ W $\times$ H $= 6$ cm $\times$ 6 cm $\times$ 1 mm. As shown in Fig. 12 (b), each SS plate was placed in a 6.2 cm $\times$ 6.2 cm interior of a 3D printed frame attached to the PANDA 11 machine's 27.9 cm $\times$ 27.9 cm build plate, where the plate rested on four thermal-insulating washers (Misumi Part # DJW10–3–3 with thermal conductivity of 0.24 W/(mK)). The washers minimized conductive heat transfer between the SS plate and the build plate. This allowed the
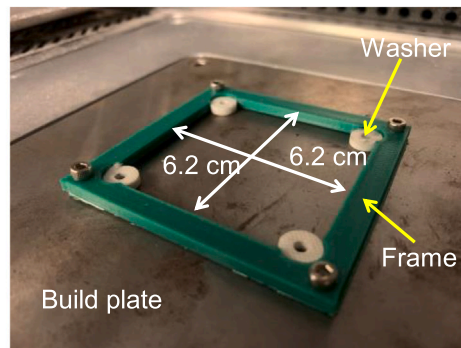

(a)

(b)

Fig. 12. (a) PANDA 11 open architecture LPBF machine; and (b) fixture used for positioning plates during scanning experiments. The plates sat on the four insulating washers within the 6.2 cm $\times$ 6.2 cm opening of the frame.
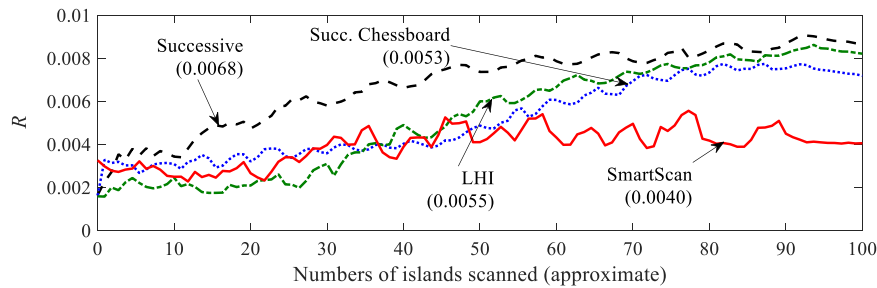
Fig. 13. Experimentally measured thermal uniformity metric (*R*) for different scan sequences as a function of the number of islands scanned (approximately). The numbers in parenthesis show the mean value of *R* for each scan sequence.

experimental setup to better match the simulation setup of Section 3, which did not include heat transfer to the build plate. The SS plates were not constrained in any way during the experiments, allowing them to deform freely under the thermal stresses induced by the laser marking process. The process parameters used to mark each plate are listed in Table 1, which are the exact same parameters as used in the simulations. An additional parameter not included in Table 1 is the laser jump speed which was 6000 mm/s.

Each plate was scanned twice using the sequence being evaluated to amplify the thermal deformations induced in the plate. After the first scan was performed, the plate was allowed to cool to the ambient temperature before it was re-scanned. Using the IR camera, the apparent temperature of the plates was recorded at 4 frames per second during each experiment and the results exported as CSV files for processing in MATLAB. The recorded temperatures are apparent because the emissivity of the SS plate was not experimentally calibrated. It was selected as 0.35, based on typical values for stainless steel. However, actual emissivity is highly dependent on a variety of factors hence it must be calibrated carefully to obtain accurate absolute temperatures. However, for the purposes of this paper, apparent temperatures are sufficient. This is because it is the relative, not the absolute, values of the temperatures that are important for evaluating temperature distribution.

To measure their deformations, the marked plates were each laser scanned using a Romer Absolute Arm (Hexagon AB, Sweden) model # 7525SI with a scanning accuracy of 63 μm. The plates were placed on a

flat table upside down and their bottom surfaces scanned to determine their deformed shapes. The resulting point clouds were exported to MATLAB for processing.

4.2. Comparative Evaluation of Thermal Uniformity, Deformations and Scanning Time

4.2.1. Case 1: Island Scan Pattern

The same island scan sequences discussed in Section 3 were evaluated in experiments. Fig. 13 shows the *R* values of the tested sequences, calculated from the measured apparent temperatures, as a function of time. The time axis is normalized by the total number of islands scanned such that the end time corresponds to the completion of the 100th island and the intermediary time steps approximate the number of islands scanned at each time step. Similar to the simulations, the Successive sequence showed the least uniform temperature distribution while the proposed SmartScan sequence exhibited the most uniform temperature distribution throughout the scanning process. The quantitative discrepancies between the *R* plots in simulations and experiments are attributable to various approximations made in simulation model (e.g., ignoring the jump time and latent heat effects), and the use of apparent instead of absolute temperatures. Nonetheless, the qualitative results are in general agreement between simulation and experiments. The mean *R* value for SmartScan was 1.7, 1.3 and 1.4 times (or 41%, 25% and 27%) lower than those of the Successive, Successive Chessboard and LHI
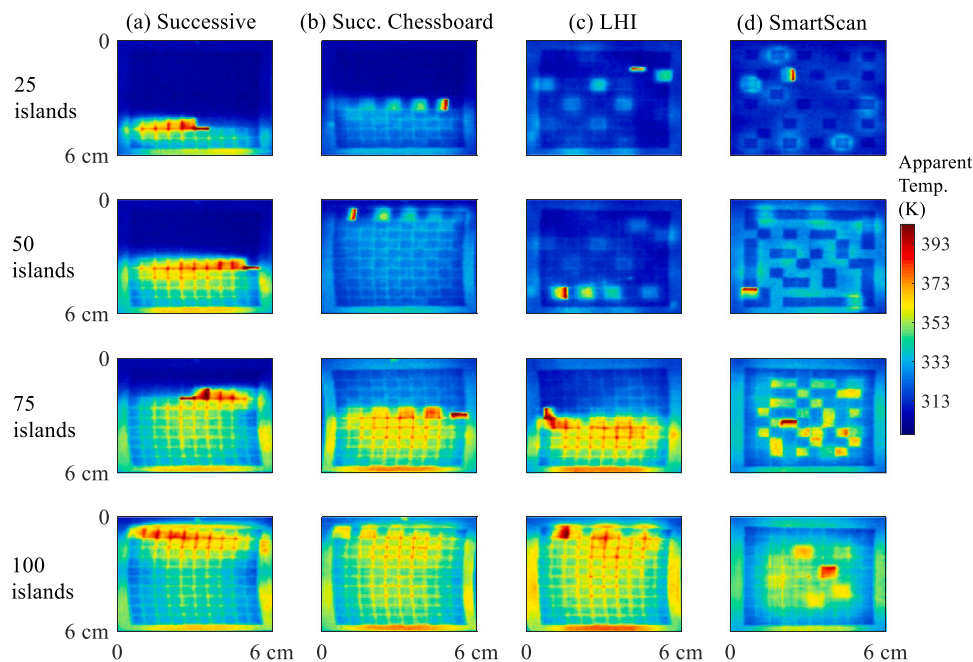

Fig. 14. Experimentally measured temperature distribution of 6 cm × 6 cm AISI 316 L stainless steel plate for the island scan pattern at four instances during the scanning process. The proposed SmartScan shows more uniform temperature distribution than the competing heuristic approaches.
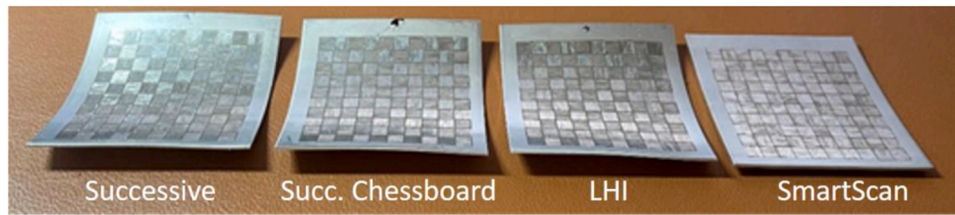
Fig. 15. Picture of 6 cm × 6 cm AISI 316 L stainless steel plates after laser marking using the four island scan sequences under study. Observe that the plate marked using the proposed SmartScan scan sequence shows much less deformation than those marked using the competing heuristic approaches.
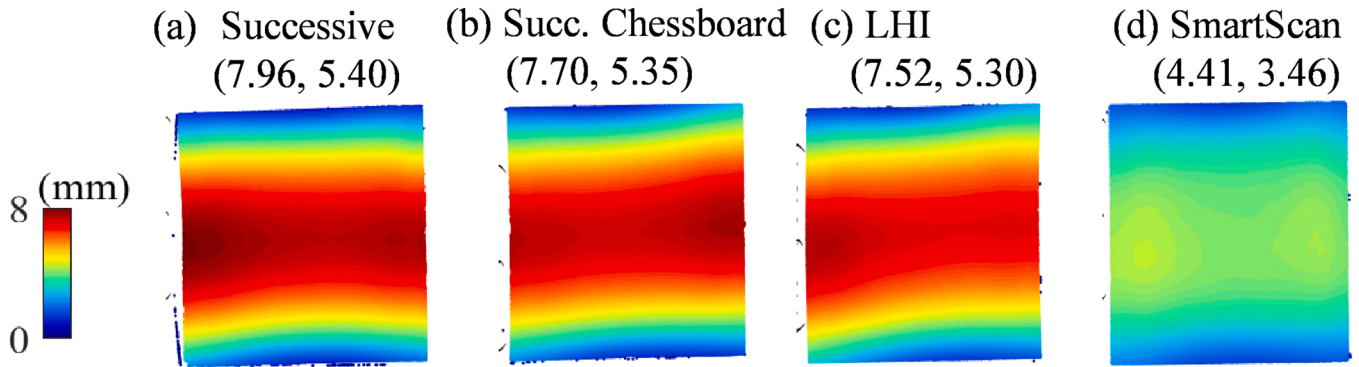

Fig. 16. Measured deformation profiles of 6 cm × 6 cm AISI 316 L stainless steel plates using the four island scan sequences under study. The numbers in parenthesis are respectively the maximum and mean deformations of each plate in mm. Notice that the proposed SmartScan shows significantly lower deformations than the competing heuristic approaches. The plates were scanned upside down.

Table 4
Scanning time for island scan sequences.

Scanning Sequence	Scanning time (s)
Successive	25.7
Successive chessboard	25.7
LHI	25.9
SmartScan (proposed)	26.4

sequences. This confirms the findings in the simulations that the proposed SmartScan sequence yields better thermal uniformity compared to the competing approaches. This fact is confirmed by Fig. 14 which shows the thermal distribution of the four approaches at four instances – after 25, 50, 75 and 100 islands were scanned (see the supplemental information for.gif animations of the temperature distribution of each sequence as a function of time).

Fig. 15 shows a picture of the scanned plates while Fig. 16 shows the deformation profiles of each of the plates. The maximum deformation of the plate marked using SmartScan is 1.8, 1.75 and 1.7 times (or 45%, 43% and 41%) lower than those of the plates marked using Successive,

Successive Chessboard and LHI, respectively. Similarly, the mean deformation of the plate marked using SmartScan is 1.56, 1.55 and 1.53 times (or 36%, 35% and 35%) lower than those of the plates marked using Successive, Successive Chessboard and LHI, respectively. These clearly demonstrates that the proposed SmartScan generates significantly lower internal thermal stresses than the competing approaches.

The scanning (cycle) time for executing each sequence on the PANDA 11 machine is listed in Table 4. The proposed SmartScan took 2.7% longer than both the Successive and Successive Chessboard, and 1.9% longer than LHI due to the fact that it required the laser to jump around more than the competing methods. This shows that the performance improvement of SmartScan did not come at the expense of significantly increased scanning time compared to the heuristic approaches.

4.2.2. Case 2: Stripe Scan Pattern

The stripe scan sequences discussed in Section 3 were evaluated in experiments. Fig. 17 shows the R values of the tested sequences, calculated from the measured apparent temperatures, as a function of time. The time axis is normalized by the total number of islands scanned such that the end time corresponds to the completion of the 250th stripe, and the intermediary time steps approximate the number of stripes scanned
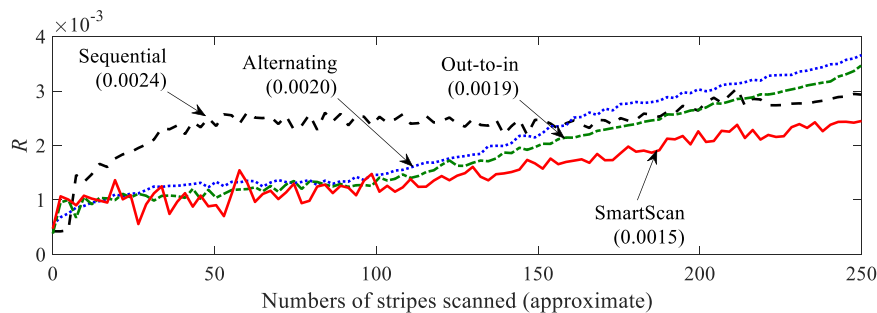

Fig. 17. Experimentally measured thermal uniformity metric (R) for different scan sequences as a function of the number of stripes scanned (approximately). The numbers in parenthesis show the mean of R for each scan sequence.
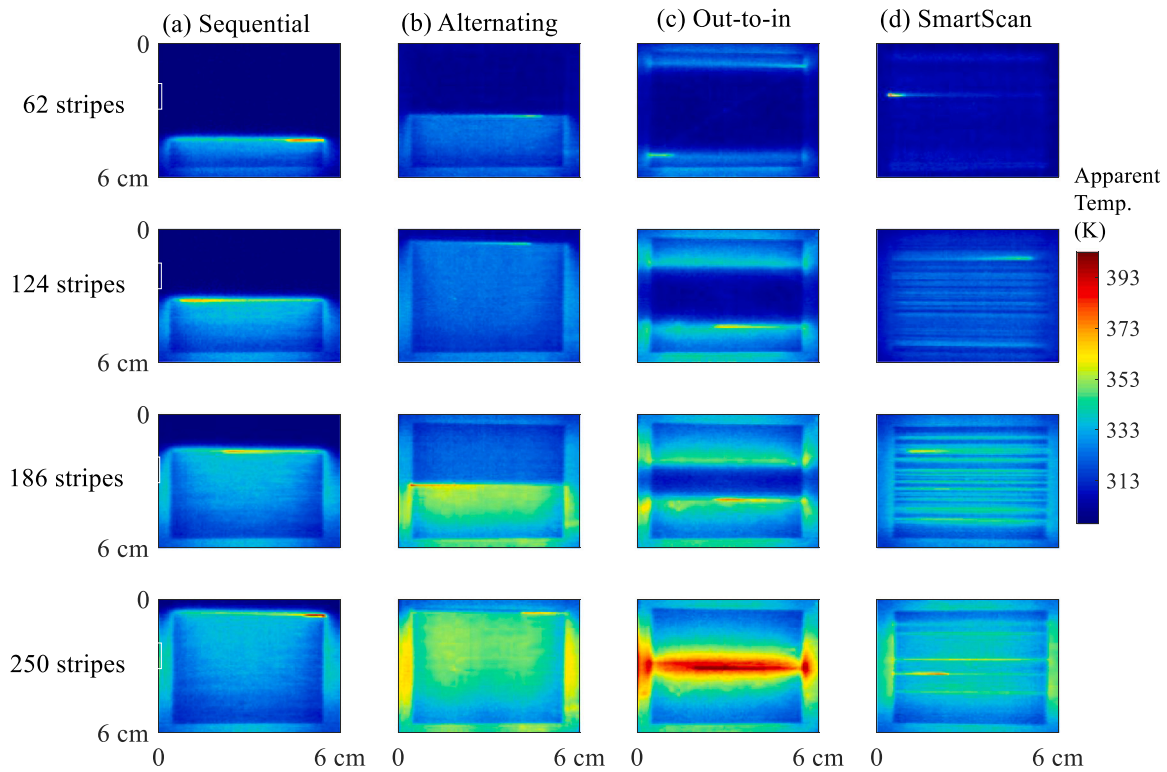
Fig. 18. Experimentally measured temperature distribution of 6 cm × 6 cm AISI 316 L stainless steel plate for the stripe scan pattern at four instances during the scanning process. The proposed SmartScan shows more uniform temperature distribution than the competing heuristic approaches.
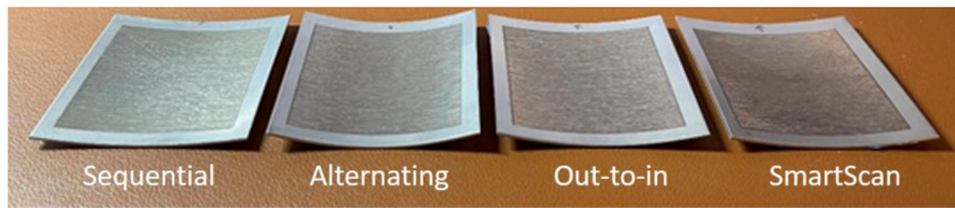

Fig. 19. Picture of 6 cm × 6 cm AISI 316 L stainless steel plates after laser marking using the four stripe scan sequences under study. Observe that the proposed SmartScan scan sequence shows less deformation than the competing heuristic approaches.
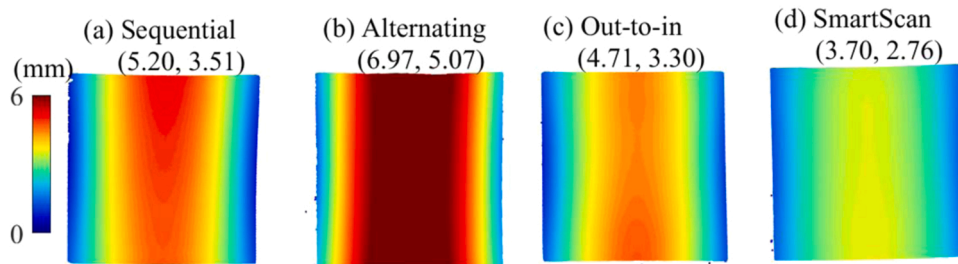

Fig. 20. Measured deformation profiles of 6 cm × 6 cm AISI 316 L stainless steel plates using the four stripe scan sequences under study. The numbers in parenthesis are respectively the maximum and mean deformations for each plate. Notice that the proposed SmartScan shows significantly lower deformations than the competing heuristic approaches. The plates were scanned upside down.

at each time step. Similar to the simulations, the Sequential method shows the least uniform temperature distribution while the proposed SmartScan sequence generally exhibits the most uniform temperature distribution throughout the scanning process. The mean *R* value for SmartScan is 1.6, 1.3 and 1.3 times (or 38%, 25% and 21%) lower than those of the Sequential, Alternating and Out-to-in approaches, respectively. This confirms the findings in the simulations that the proposed

SmartScan sequence yields better thermal uniformity compared to the competing approaches. This fact is confirmed by Fig. 18 which shows the thermal distribution of the four approaches at four instances – after 62, 124, 186 and 250 stripes were scanned (see the supplemental information for.gif animations of the temperature distribution of each sequence as a function of time). SmartScan generally shows better temperature distribution than the heuristic approaches at all instances.

Table 5
Scanning time for stripe scan sequences.

Scanning Sequence	Scanning time (s)
Sequential	21.7
Alternating	23.4
Out-to-in	23.7
SmartScan (proposed)	23.6

Fig. 19 shows a picture of the scanned plates while Fig. 20 shows the deformation profiles of each of the plates. The maximum deformation of the plate marked using SmartScan is 1.4, 1.9 and 1.3 times (or 29%, 47% and 21%) lower than those of the plates marked using the Sequential, Alternating and Out-to-in approaches, respectively. Similarly, the mean deformation of the plate marked using SmartScan is 1.3, 1.8 and 1.2 times (or 21%, 46% and 16%) lower than those of the plates marked using the Sequential, Alternating and Out-to-in approaches, respectively. These clearly demonstrates that the proposed SmartScan generates significantly lower internal thermal stresses than the competing heuristic approaches.

The scanning (cycle) time for executing each sequence on the PANDA 11 machine is listed in Table 5. The proposed SmartScan takes 8.8% and 0.9% longer than the sequential and alternating methods, respectively, and saves 0.4% time compared to the out-to-in approach. This shows that the performance improvement of SmartScan does not necessarily come at the expense of significantly increased scanning time compared to heuristic approaches. In some cases, it could both reduce scanning time and improve thermal uniformity.

5. Conclusions and future work

This paper has presented a new approach, called SmartScan, for optimally determining scan sequences in powder bed fusion (PBF) additive manufacturing in order to attain more uniform temperature distribution, reduced residual stresses and deformations. What makes SmartScan unique is that it is an intelligent approach that is model-based, optimization-driven and computationally-efficient enough to be executed online. It is paradigm shift away from existing approaches for determining scan sequences which depend on trial-and-error or geometry-based heuristics. Our first attempt at SmartScan, detailed in this paper, is achieved using a simplified finite difference model of PBF consisting of only heat conduction and convection. The model order is reduced using radial basis functions and the optimal sequences that minimize a thermal uniformity metric are determined efficiently using control theory.

Simulations and experiments involving laser marking of AISI 316 L stainless steel plates using stripe and island scan patterns show that SmartScan drastically improves thermal uniformity and thermal-stress induced deformations compared to well-known heuristic approaches. Moreover, it is computationally efficient enough to be run online and is reasonably robust to errors in model parameters. The use of a thermal model based on the finite difference method makes SmartScan amenable to a wide range of geometries and boundary conditions encountered in PBF. Moreover, even though SmartScan was discussed in the context of stripe and island scan patterns, which are very popular in practice, it is applicable to a variety of other scan patterns with repeating features, like fractals [34] and varying-helix islands [35]. However, a key limitation is that the model used for SmartScan considers only one scanned layer and does not include the physics of the powder melting process. Hence, it is currently only applicable to the layer re-scanning process in PBF [27], or the plate marking process often used to evaluate the effects of heat accumulation and scanning strategies in PBF, e.g., [5,28]. Future work will be focused on improving the SmartScan approach by incorporating more advanced models of PBF, e.g., powder melting related phenomena, using a combination of physics-based and data-driven approaches. Multiple scanned layers will also be considered and the

SmartScan approach will be implemented online. These improvements in the models used in SmartScan will likely necessitate new scan sequence optimization techniques to handle their increased complexities while maintaining high computational efficiency. Also, the SmartScan approach (see Fig. 5) is a greedy optimization approach and in future, limited preview horizons will be considered to find an optimal global solution. Also, the efficacy of the SmartScan approach when the substrate is preheated will be studied in future work. In addition, future work will seek to understand how SmartScan affects microstructure, porosity, and other defects/properties of the manufactured part that are (indirectly) influenced by scan sequence. For example, the direction of scanning relative to the gas flow, spatter and plume cloud formation within the build chamber may affect void formation and porosity, hence, must be considered.

CRediT authorship contribution statement

Keval S. Ramani: Conceptualization, Methodology, Formal analysis, Validation, Writing – original draft, Writing – review & editing. **Chuan He:** Methodology, Formal analysis, Validation, Data curation. **Yueh-Lin Tsai:** Methodology, Validation, Data curation. **Chinedum E. Okwudire:** Conceptualization, Methodology, Validation, Writing – original draft, Writing – review & editing, Supervision, Funding acquisition.

Declaration of Competing Interest

The authors declare the following financial interests/personal relationships which may be considered as potential competing interests, The Regents of the University of Michigan have applied for patents related to SmartScan.

APPENDIX

The full sequences for the LHI and SmartScan shown in Fig. 6(b) and (c) based on the island numbering template in Fig. 6(a) are as follows:
LHI:
1,91,10,100,45,52,86,5,41,23,27,63,31,67,97,3,7,21,25,43,47,61,65,-71,88,12,15,17,19,33,35,37,39,55,57,59,77,79,83,94,2,4,6,8,9,11,13,-14,16,18,20,22,24,26,28,29,30,32,34,36,38,40,42,44,46,48,49,50,51, 53,54,56, 58,60,62,64,66,68,69,70,72,73,74,75,76,78,80,81,82,84,85, 87,89,90,92,93,95,96,98 and 99.
SmartScan:
49,79,19,93,6,10,45,96,75,41,71,100,27,91,24,68,30,1,58,4,50,98,8,-61,77,21,55,94,34,81,70,38,11,92,2,5,7,25,97,60,74,31,53,57,40,95,-90,99,9,20,80,78,51,3,28,46,65,37,15,88,42,67,85,48,69,12,22,82,17, 62,89,14,32,35,44,87,84,64,66,39,18,52,16,59,13,72,29,83,86,47,36,-56,23,63,73,43,26,33,76 and 54.

The full sequence for SmartScan shown in Fig. 9, based on stripes numbered sequentially from 1 at the bottom edge to 250 at the top edge of the scanned area, is as follows:

250,1,27,51,75,224,200,176,152,12,244,38,62,86,110,134,218,194, 13,238,39,63,87,111,159,183,207,231,6,26,50,74,98,122,245,219,-195,171,7,33,57,81,239,212,188,164,140,116,8,32,56,236,213,189,-165,141,93, 9,45,69,237,201,177,153,129,105,21,44,225,249,2,182,-206,158,135,99,15,230,68,248,117,170,146,3,25,92,243,221,128,147, 14,36,80,104,242,220,123,20,42,202,233,4,60,24,215,247,191,-43,226,19,72,167,246,214,37,5,232,18,190,61,209,84,227,30,10,166-

,48,240,208,73,31,11,184,228,49,203,161,131,241,22,66,46,90,196,-216,172,142,234,23,55,109,89,197,217,173,143,235,16,34,54,85,-115,178,198,154,222,17,35,67,97,179,199,155,223,130,28,108,76,-58,185,205,149,229,29,96,52,120,78,168,148,192,210,41,107,127,83,65,169,151,193,211,47,103,71,126,180,160,204,40,94,114,70,138,-181,163,53,95,113,133,77,186,156,59,91,121,139,174,106,64,157,-88,132,187,119,162,79,101,145,125,175,82,102,150,118,136,100,124,144,112 and 137.

Appendix A. Supporting information

Supplementary data associated with this article can be found in the online version at doi:10.1016/j.addma.2022.102643.

References

[1] M. Mani, B.M. Lane, M.A. Donmez, S.C. Feng, S.P. Moylan, A Review on Measurement Science Needs for Real-Time Control of Additive Manufacturing Metal Powder Bed Fusion Processes, Int. J. Prod. Res. 55 (5) (2017) 1400–1418.

[2] Q. Wang, P.P. Michaleris, A.R. Nassar, J.E. Irwin, Y. Ren, C.B. Stutzman, Model-Based Feedforward Control of Laser Powder Bed Fusion Additive Manufacturing, Addit. Manuf. 31 (2020), 100985.

[3] G. Tapia, A. Elwany, A Review on Process Monitoring and Control in Metal-Based Additive Manufacturing, J. Manuf. Sci. Eng. 136 (6) (2014).

[4] L. Parry, I. Ashcroft, R.D. Wildman, Understanding the Effect of Laser Scan Strategy on Residual Stress in Selective Laser Melting through Thermo-Mechanical Simulation, Addit. Manuf. 12 (2016) 1–15.

[5] L. Mugwagwa, D. Dimitrov, S. Matope, I. Yadroitsev, Evaluation of the Impact of Scanning Strategies on Residual Stresses in Selective Laser Melting, Int. J. Adv. Manuf. Technol. 102 (5–8) (2019) 2441–2450.

[6] Q. Chen, H. Taylor, A. Takezawa, X. Liang, X. Jimenez, R. Wicker, A.C. To, Island Scanning Pattern Optimization for Residual Deformation Mitigation in Laser Powder Bed Fusion via Sequential Inherent Strain Method and Sensitivity Analysis, Addit. Manuf. 46 (2021), 102116.

[7] Price, S., Lydon, J., Cooper, K., and Chou, K., 2013, Experimental Temperature Analysis of Powder-Based Electron Beam Additive Manufacturing, 24th Annual International Solid Freeform Fabrication Symposium, Austin, TX, pp. 162–173.

[8] J. Robinson, I. Ashton, P. Fox, E. Jones, C. Sutcliffe, Determination of the Effect of Scan Strategy on Residual Stress in Laser Powder Bed Fusion Additive Manufacturing, Addit. Manuf. 23 (2018) 13–24.

[9] L. Parry, I. Ashcroft, R. Wildman, Geometrical Effects on Residual Stress in Selective Laser Melting, Addit. Manuf. 25 (2019) 166–175.

[10] R. McCann, M.A. Obeidi, C. Hughes, E. McCarthy, D.S. Egan, R.K. Vijayaraghavan, A.M. Joshi, V.A. Garzon, D.P. Dowling, P.J. McNally, D. Brabazon, In-Situ Sensing, Process Monitoring and Machine Control in Laser Powder Bed Fusion: A Review, Addit. Manuf. 45 (2021), 102058.

[11] Kruth, J.-P., Duflou, J., Mercelis, P., Van Vaerenbergh, J., Craeghs, T., and De Keuster, J., 2007, On-Line Monitoring and Process Control in Selective Laser Melting and Laser Cutting, *Proceedings of the 5th Lane Conference, Laser Assisted Net Shape Engineering*, pp. 23–37.

[12] S. Berumen, F. Bechmann, S. Lindner, J.-P. Kruth, T. Craeghs, Quality Control of Laser-and Powder Bed-Based Additive Manufacturing (AM) Technologies, Phys. Procedia 5 (2010) 617–622.

[13] Wang, X., Lough, C.S., Bristow, D.A., Landers, R.G., and Kinzel, E.C., 2020, "A Layer-to-Layer Control-Oriented Model for Selective Laser Melting," 2020 American Control Conference (ACC), pp. 481–486.

[14] J.E. Irwin, Q. Wang, P.P. Michaleris, A.R. Nassar, Y. Ren, C.B. Stutzman, Iterative Simulation-Based Techniques for Control of Laser Powder Bed Fusion Additive Manufacturing, Addit. Manuf. 46 (2021), 102078.

[15] F. Ogoke, A.B. Farimani, Thermal Control of Laser Powder Bed Fusion Using Deep Reinforcement Learning, Addit. Manuf. 46 (2021), 102033.

[16] T. Phillips, S. Fish, J. Beaman, Development of an Automated Laser Control System for Improving Temperature Uniformity and Controlling Component Strength in Selective Laser Sintering, Addit. Manuf. 24 (2018) 316–322.

[17] T. Phillips, T. Ricker, S. Fish, J. Beaman, Design of a Laser Control System with Continuously Variable Power and Its Application in Additive Manufacturing, Addit. Manuf. 34 (2020), 101173.

[18] C. Li, C. Fu, Y. Guo, F. Fang, A Multiscale Modeling Approach for Fast Prediction of Part Distortion in Selective Laser Melting, J. Mater. Process. Technol. 229 (2016) 703–712.

[19] Malekipour, E., 2018, "Innovative Tessellation Algorithm for Generating More Uniform Temperature Distribution in the Powder-Bed Fusion Process," Master's Thesis Purdue Univ.

[20] D. Ramos, F. Belblidia, J. Sienz, New Scanning Strategy to Reduce Warpage in Additive Manufacturing, Addit. Manuf. 28 (2019) 554–564.

[21] J.-P. Kruth, L. Froyen, J. Van Vaerenbergh, P. Mercelis, M. Rombouts, B. Lauwers, Selective Laser Melting of Iron-Based Powder, J. Mater. Process. Technol. 149 (1–3) (2004) 616–622.

[22] E. Malekipour, H. Valladares, Y. Shin, H. El-Mounayri, Optimization of Chessboard Scanning Strategy Using Genetic Algorithm in Multi-Laser Additive Manufacturing Process, ASME Int. Mech. Eng. Congr. Expo. (2020). V02AT02A054.

[23] C. Reiff, W. Bubeck, D. Krawczyk, M. Steeb, A. Lechler, A. Verl, Learning Feedforward Control for Laser Powder Bed Fusion, Procedia CIRP 96 (2021) 127–132.

[24] Ramani, K.S., Malekipour, E., and Okwudire, C.E., 2021, Toward Intelligent Online Scan Sequence Optimization for Uniform Temperature Distribution in LPBF Additive Manufacturing, *Proceedings of the MSEC 2021 Manufacturing Science and Engineering Conference.*

[25] Ramani, K.S., and Okwudire, C.E., 2021, "Intelligent Scan Sequence Optimization for Uniform Temperature Distribution in Laser Powder Bed Fusion Using a Control Theoretic Approach," *Modeling, Estimation and Control Conference (MECC 2021) (Accepted).*

[26] G.E. Fasshauer, Meshfree Approximation Methods with MATLAB, World Scientific,, 2007.

[27] H. Ali, H. Ghadbeigi, K. Mumtaz, Effect of Scanning Strategies on Residual Stress and Mechanical Properties of Selective Laser Melted Ti6Al4V, Mater. Sci. Eng. A 712 (2018) 175–187.

[28] H. Yeung, B. Lane, A Residual Heat Compensation Based Scan Strategy for Powder Bed Fusion Additive Manufacturing, Manuf. Lett. 25 (2020) 56–59.

[29] J. Ning, D.E. Sievers, H. Garmestani, S.Y. Liang, Analytical Thermal Modeling of Metal Additive Manufacturing by Heat Sink Solution, in: Materials (Basel), 12, 2019, p. 2568.

[30] M.R. Yavari, K.D. Cole, P. Rao, Thermal Modeling in Metal Additive Manufacturing Using Graph Theory, J. Manuf. Sci. Eng. 141 (7) (2019).

[31] T. Yener, S.C. Yener, R. Mutlu, Convection Coefficient Estimation of Still Air Using an Infrared Thermometer and Curve-Fitting, J. Eng. Technol. Appl. Sci. 4 (2) (2019) 95–103.

[32] D. Bergstrom, J. Powell, A. Kaplan, The Absorptance of Steels to Nd: YLF and Nd: YAG Laser Light at Room Temperature, Appl. Surf. Sci. 253 (11) (2007) 5017–5028.

[33] K.C. Mills, Recommended Values of Thermophysical Properties for Selected Commercial Alloys, Woodhead Publishing,, 2002.

[34] S. Catchpole-Smith, N. Aboulkhair, L. Parry, C. Tuck, I. Ashcroft, A. Clare, Fractal Scan Strategies for Selective Laser Melting of 'Unweldable' Nickel Superalloys, Addit. Manuf. 15 (2017) 113–122.

[35] D. Hagedorn-Hansen, M. Bezuidenhout, D. Dimitrov, G. Oosthuizen, The Effects of Selective Laser Melting Scan Strategies on Deviation of Hybrid Parts, South Afr. J. Ind. Eng. 28 (3) (2017) 200–212.